6-2016

Femtosecond gas phase electron diffraction with MeV electrons

Jie Yang
University of Nebraska-Lincoln

Markus Guehr
Potsdam University, Potsdam, mguehr@uni-potsdam.de

Theodore Vecchione
SLAC National Accelerator Laboratory, tvecchio@slac.stanford.edu

Matthew S. Robinson
University of Nebraska-Lincoln, matthew.robinson@unl.edu

Renkai Li
SLAC National Accelerator Laboratory, lrk@slac.stanford.edu

See next page for additional authors

Authors
Jie Yang, Markus Guehr, Theodore Vecchione, Matthew S. Robinson, Renkai Li, Nick Hartmann, Xiaozhe Shen, Ryan Coffee, Jeff Corbett, Alan Fry, Kelly Gaffney, Tais Gorkhover, Carsten Hast, Keith Jobe, Igor Makasyuk, Alexander Reid, Joseph Robinson, Sharon Vetter, Fenglin Wang, Stephen Weathersby, Charles Yoneda, Xijie Wang, and Martin Centurion

Faraday Discussions

Cite this: DOI: 10.1039/c6fd00071a

PAPER

Femtosecond gas phase electron diffraction with MeV electrons

Jie Yang,[a] Markus Guehr,[bc] Theodore Vecchione,[b] Matthew S. Robinson,[a] Renkai Li,[b] Nick Hartmann,[b] Xiaozhe Shen,[b] Ryan Coffee,[b] Jeff Corbett,[b] Alan Fry,[b] Kelly Gaffney,[b] Tais Gorkhover,[b] Carsten Hast,[b] Keith Jobe,[b] Igor Makasyuk,[b] Alexander Reid,[b] Joseph Robinson,[b] Sharon Vetter,[b] Fenglin Wang,[b] Stephen Weathersby,[b] Charles Yoneda,[b] Xijie Wang[b] and Martin Centurion*[a]

Received 10th April 2016, Accepted 2nd June 2016
DOI: 10.1039/c6fd00071a

We present results on ultrafast gas electron diffraction (UGED) experiments with femtosecond resolution using the MeV electron gun at SLAC National Accelerator Laboratory. UGED is a promising method to investigate molecular dynamics in the gas phase because electron pulses can probe the structure with a high spatial resolution. Until recently, however, it was not possible for UGED to reach the relevant timescale for the motion of the nuclei during a molecular reaction. Using MeV electron pulses has allowed us to overcome the main challenges in reaching femtosecond resolution, namely delivering short electron pulses on a gas target, overcoming the effect of velocity mismatch between pump laser pulses and the probe electron pulses, and maintaining a low timing jitter. At electron kinetic energies above 3 MeV, the velocity mismatch between laser and electron pulses becomes negligible. The relativistic electrons are also less susceptible to temporal broadening due to the Coulomb force. One of the challenges of diffraction with relativistic electrons is that the small de Broglie wavelength results in very small diffraction angles. In this paper we describe the new setup and its characterization, including capturing static diffraction patterns of molecules in the gas phase, finding time-zero with sub-picosecond accuracy and first time-resolved diffraction experiments. The new device can achieve a temporal resolution of 100 fs root-mean-square, and sub-angstrom spatial resolution. The collimation of the beam is sufficient to measure the diffraction pattern, and the transverse coherence is on the order of 2 nm. Currently, the temporal resolution is limited both by the pulse duration of the electron pulse on target and by the timing jitter, while the spatial resolution is limited by the average electron beam current and

[a]*University of Nebraska-Lincoln, 855 N 16th Street, Lincoln, Nebraska 68588, USA. E-mail: martin.centurion@unl.edu*

[b]*SLAC National Accelerator Laboratory, Menlo Park, CA 94025, USA*

[c]*Physics and Astronomy, Potsdam University, Potsdam, 14476, Germany*

the signal-to-noise ratio of the detection system. We also discuss plans for improving both the temporal resolution and the spatial resolution.

1. Introduction

Ultrafast gas electron diffraction (UGED) can in principle provide sufficient temporal and spatial resolution to observe bond length changes in isolated molecules during a photo-induced reaction. In order to capture the trajectory of individual atoms during a reaction, femtosecond resolution is required. Recent experiments using relativistic electron pulses with MeV energy have succeeded in reaching a temporal resolution of 230 fs full-width at half maximum (FWHM) or 100 fs root-mean-squared (RMS).[1] In this manuscript we will expand on the previously reported results. Additional information is provided about the operation of the MeV gun during the gas phase experiments, and the detection system is described in detail. A crucial step towards performing pump–probe experiments is to find temporal overlap between laser and electron pulses. Here we describe how we found the temporal overlap by producing a laser plasma that deflects the electron beam. We also provide additional data on the noise level of the measurements and the temporal fitting that was used to extract the temporal resolution from the rotational dynamics.

1.1. Background

Time resolved electron diffraction has been applied to gas phase samples over the years with resolutions from microseconds to nanoseconds.[2,3] The promise of UGED was demonstrated by the Zewail group when they were able to retrieve the structure of transient states with few-picosecond resolution.[4–6] Over the last 15 years, though, the achievable resolution in UGED was limited to the picosecond scale.[7–9]

While capturing the motion of atoms in isolated molecules has remained elusive, this goal has been achieved for crystallized molecules by the Miller group.[10,11] In condensed matter ultrafast electron diffraction (UED), femtosecond dynamics have been observed using compact electron guns[12,13] where the charge per pulse is limited and the source-to-target distance is kept very short to reduce the Coulomb broadening of the electron pulses. An alternative approach has been the use of radio-frequency (RF) cavities to deliver temporally compressed electron pulses at the sample position.[14–16] These methods have so far not been successfully implemented on UGED, although they could be applied if some technical challenges are overcome. For example, compact guns require a high vacuum on the photocathode to avoid discharges, while the pressure near the gas target is typically much higher. For RF compression of keV electrons, the synchronization between the RF compression fields and the laser pulses has limited the available temporal resolution to ~300 fs.

Several other methods are available to probe molecules in the gas phase with high spatio-temporal resolution using X-ray and laser sources. The first is hard X-ray diffraction using femtosecond pulses from an X-ray free-electron laser (X-FEL). X-ray diffraction experiments on the ring-opening reaction of CHD were recently carried out with temporal resolution of 80 fs, where the transient structures were retrieved by comparing the experimental results with simulations.[17]

Molecular structures can also be probed using femtosecond X-ray photoelectron diffraction[18] and laser-induced electron diffraction.[19–21] In these methods the molecule is ionized either by an X-ray pulse or an intense laser pulse, and the emitted electron diffracts from the parent molecules. The advantage of UGED compared with these methods is that the probing electrons are not generated on the molecule itself, so knowledge of the ionization process is not required. In addition, UGED does not expose the molecule to strong laser fields. Here we show how the challenges associated with achieving high temporal resolution in UGED can be overcome using electron pulses accelerated to MeV energy.

1.2. Spatial and temporal resolution in UGED

The spatial resolution δ is the smallest feature which can be resolved in an object. It is determined by the de Broglie wavelength of the electrons and the range of diffraction angles that are captured. For small diffraction angles, the resolution can be written as

$$\delta = \frac{\lambda}{\theta_{\max}},$$

where λ is the de Broglie wavelength of the electron beam, and $\theta_{\max}$ is the maximum scattering angle captured in the diffraction pattern. For a relativistic electron beam with a kinetic energy of 3.7 MeV, λ is 0.30 pm. In UGED, the interatomic distances in a molecule can often be determined with an accuracy significantly higher than the spatial resolution, provided that distances do not overlap within the resolution, or that there is some prior knowledge of the structure, such as the number of atoms in the molecule. The resolution determines the width of each peak corresponding to an atomic position (or interatomic distance) in the retrieved object, while the accuracy determines how accurately the center of each peak can be found. The spatial resolution of a retrieved object is mostly limited by the signal-to-noise ratio (SNR) in the experiment. The differential scattering cross section drops rapidly with scattering angle, thus detecting electrons at higher scattering angles requires higher signal levels. Spatial resolution can be improved by increasing the beam current, the integration time, or the sample density, or by reducing the detector noise.

The maximum size of an object that can be measured is determined by the transverse coherence length of the electron beam $L_c = \lambda/2\pi\Delta\phi$, where $\Delta\phi$ is the angular divergence of the electron beam. The transverse coherence of the MeV beam used in our experiments is 1.7 nm. The transverse coherence of a beam can be increased by expanding the beam or by using apertures, at the expense of beam intensity. The ratio of the transverse coherence length to the beam size depends on the emittance of the beam.

The temporal resolution of a UED experiment, where a sample is excited by a laser pulse and probed by an electron pulse, can be approximated as:

$$\tau_{\mathrm{EXP}} = \sqrt{{\tau_{\mathrm{laser}}}^2 + {\tau_{\mathrm{electron}}}^2 + {\tau_{\mathrm{TOA}}}^2 + {\tau_{\mathrm{VM}}}^2} \quad (1)$$

where τ_{laser} is the duration of the laser pulse, τ_{electron} is the duration of the electron pulse, τ_{TOA} is a measure of the jitter and drift in the relative time of arrival (TOA) between laser and electron pulses at the sample, and τ_{VM} accounts for the effect of the velocity mismatch (VM) of the laser and electron pulses as they

traverse the sample. The contribution of the laser pulse duration to the overall resolution is minimal, since laser pulses with a duration of 30 fs or less can be made routinely. The electron pulses are generated by photoemission, and can be as short as the laser pulse at the point of emission, but the pulse duration rapidly increases as the pulse is accelerated and propagates to the sample. This broadening is caused by the initial energy spread of the photoelectrons and by the Coulomb force (space charge effect). Several methods are available for delivering short pulses on a target: placing the sample very close to the source, limiting the number of electrons per pulse, and using time-dependent fields to recompress the pulses. The jitter in the TOA arises from temporal variations in the acceleration electric field in the gun and/or the RF compression field. The VM results from the fact that laser and electron pulses traverse the sample at different velocities.[22] The VM effect can be minimized by using thin samples, by tilting the laser pulse front,[23,24] or by using relativistic electron pulses.[25–29] For condensed matter experiments in transmission, the sample is usually thinner than a micrometer, resulting in negligible blurring due to velocity mismatch.

We identify three unique challenges towards achieving high spatio-temporal resolution in UGED: (i) the target density is very low. Usually, gas jets are used to deliver the sample molecules, resulting in a low column density on the order of 10^{15} molecules per cm^3, and a high electron beam current is needed to have a sufficient number of scattering events. This often results in a trade-off between spatial and temporal resolution, since the duration of the pulse will elongate with increasing charge.

(ii) The sample molecules in the gas beam are randomly oriented, which reduces the amount of information that is encoded in the diffraction pattern due to the angular averaging. The result is that typically only 1D information (corresponding to the interatomic distances) can be accessed.[30] It has been shown that diffraction from aligned molecules can be used to retrieve both the distances and angles in a molecule.[7] The effects of alignment have been described elsewhere[31,32] and in this manuscript we will focus on the effects of the temporal resolution.

(iii) The gas target is typically at least 100 μm thick, which results in significant VM when non-relativistic electrons are used. For example, a 100 keV electron pulse travels with a speed of $0.55c$, where c is the speed of light in vacuum. The 100 keV electron pulse would take 1.2 ps to traverse a 200 μm sample, while the laser would take only 0.67 ps, resulting in a significant change in the relative delay between the laser and electrons throughout the sample.

2. Experimental setup

The main components of the setup are the photoelectron RF gun, the target chamber and the detection system. Here we describe each in detail.

2.1. The electron gun

Fig. 1 shows a diagram of the main parts of the setup. The experiment comprises the radiofrequency (RF) electron gun, beam transport and electron optics, the target chamber, a second beam transport line and the detector. The RF electron gun is identical to the one that drives the Linac Coherent Light Source (LCLS) at SLAC National Accelerator Laboratory. The gun is a 1.6 cell structure with

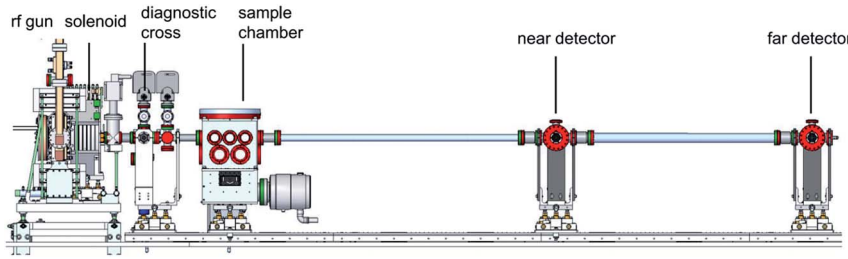

Fig. 1 Experimental layout for gas phase diffraction experiments. Electron pulses with 3.7 MeV energy are produced at the photoelectron RF gun. A series of collimators and solenoids are used to collimate the beam. The far detector position was used for gas phase experiments. Figure reprinted from ref. 25 with the permission of AIP Publishing.

2.856 GHz resonant frequency and a maximum accelerating electric field of 120 MV m^{-1}. For the UGED experiments, we operated the gun at 80 MV m^{-1} gradient and the electron beams were accelerated to 3.7 MeV kinetic energy. This beam energy was chosen to give the desired *s*-range of 1.6–15 $Å^{-1}$ in combination with the locations and dimensions of the collimators and diffraction detector.

The high acceleration gradient and high beam energy of photocathode RF guns are very effective in suppressing space-charge induced bunch lengthening. However, there are technical challenges for the control of the time or arrival jitter τ_{TOA} in RF guns. This jitter is caused by fluctuations of the RF fields amplitude and phase as well as the synchronization between the RF phase and the photocathode drive laser. In the last decade, SLAC has developed relevant key technologies mostly motivated by more precise timing control of the LCLS injector. These technologies naturally benefited the MeV UGED application as well. A top-off circuit was added to a conventional pulse-forming-network-based modulator and improved the voltage stability to <50 ppm. The modulator drives a klystron, which is the high power RF source for the gun. The amplitude and phase stabilities of the RF field are 2×10^{-4} RMS and 25 fs RMS, respectively – a factor 2–5 better than typical performances. A high-precision femtosecond timing system developed for LCLS was implemented and locks the laser and the low-level RF signal at the level of 30 fs RMS. Based on the RF and RF-laser timing performance, the estimated τ_{TOA} is 50 fs RMS for the gas-phase UED experiment.

The vacuum levels inside the UGED beamline are strongly varying. The electron gun requires $<1 \times 10^{-9}$ torr to reliably operate at high gradient with low field emission and no structure damage, while the vacuum in the sample chamber can be as high as mid-10^{-4} torr. Moreover, some gas sample species are corrosive for copper – the material the entire electron gun is made of. We separated the gun vacuum using a 50 nm thick, 1.5 mm^2 area silicon nitride (SiN) window. We experimentally verified that 75% of the electrons in the beam penetrate the SiN window with a negligible change of divergence. These electrons will contribute to the diffraction signal. The location of the SiN window, as well as other main beamline components are summarized in Table 1. A first collimator of 200 μm diameter defines the beam size at the SiN window and reduced the field emission electrons from the gun which otherwise increase the background in the diffraction pattern. A second collimator of 400 μm diameter is used to block the large-

Table 1 Gun components

Component	Position (cm)
Photocathode	0
1st collimator	55.8
SiN window	74.0
2nd collimator	144
Gas nozzle	156
Diffraction detector	458

angle scattering from the SiN window, which is much stronger than the diffraction signal from the gas molecules. The size of the 2nd collimator matched the beam block (actually a hole in the phosphor screen used for detection) of the diffraction detector. Four sets of steering magnets are used to guide the electron beam throughout the apertures along the beam line. They are located at: (i), the position of the solenoid; (ii), right after the diagnostic cross; (iii), right before the sample chamber; (iv), right after the sample chamber.

2.2. The target chamber

Fig. 2 shows a schematic view of the interaction region in the experiment. The sample molecules are introduced into the chamber using a pulsed nozzle with an exit hole of 100 μm. The nozzle operates at 120 Hz, the same repetition rate as the gun. Two differential pumping stages and the 50 nm SiN window are used to separate the gun and target chambers.

A Ti:sapphire laser with 40 fs pulses and 2 mJ energy is available to excite the sample and to trigger photoemission in the cathode. A frequency tripler is used to convert the 800 nm light into a wavelength of 267 nm for the photoemission. On the pump side, a range of wavelengths can be delivered using a dedicated optical

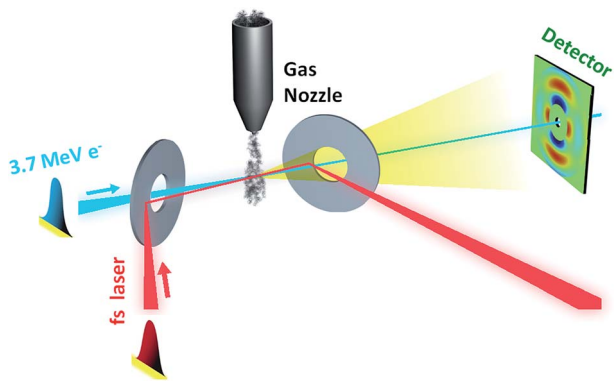

Fig. 2 Interaction region in the experimental chamber. The sample gas molecules are introduced using a pulsed nozzle. The laser beam (red) is deflected towards the target and out of the chamber using a pair of mirrors with center holes. The electron beam passes through the holes in the mirrors. The laser and electrons are nearly parallel as they traverse the sample. Figure is reproduced from ref. 1.

parametric amplifier, frequency doubler and frequency tripler. The laser is introduced into the setup using two mirrors with a hole in the center. The laser is reflected off the side of the mirrors while the electron beam passes through a hole in the center. The laser and electron pulses traverse the sample with a small angle of 5 degrees between them. The diameter of the laser beam, electron beams and gas jet are all approximately 200 μm in the interaction region. The scattered electrons exit through the hole in the second mirror and are captured by the detector.

2.3. The detector

The diffracted electrons are captured with a phosphor screen that has a hole in the center to transmit the unscattered electron beam. The size of the screen is 40 mm × 40 mm, and the center hole has a diameter of 6.3 mm to prevent saturation of the detector due to the much brighter central beam. The original phosphor screen was later replaced by a screen with a 2.9 mm hole to capture diffraction at smaller angles. The light emitted by the phosphor screen is optically coupled into an EMCCD camera. A mirror with a 6.5 mm × 9.0 mm elliptical hole, oriented at an angle of 45° to the incoming electron beam, reflects the light from the phosphor screen towards the camera. An *f*/0.85 lens is used to image the screen onto the camera.

Fig. 3a shows a schematic of the detector showing the holey phosphor screen, mirror, vacuum port, lens and EMCCD camera positions. Fig. 3b and c show diffraction patterns captured with the phosphor screens with the 6.3 mm and with the 2.9 mm diameter holes, respectively. The larger hole was originally used to avoid saturation due to the main beam, but it was later found that the smaller hole was sufficient to pass the main beam, and it also allowed for capturing more

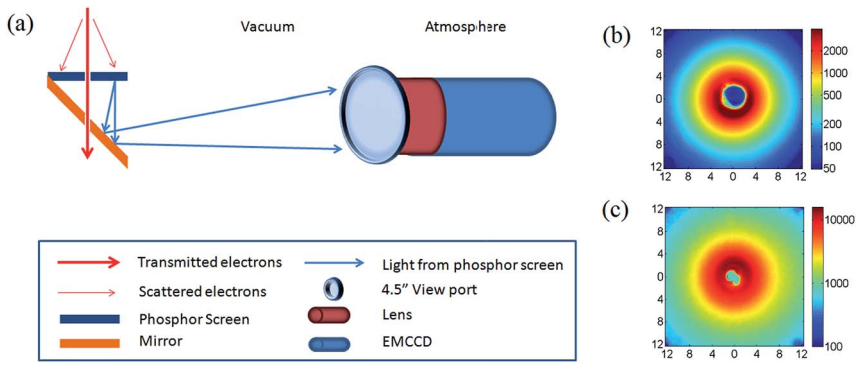

Fig. 3 (a) A sketch of the detection system. The diffraction pattern is captured by a phosphor screen, and then imaged by a 45 degree mirror and a lens on to an EMCCD camera. The main (unscattered) electron beam is transmitted through two holes in the center of the phosphor screen and mirror. A 4.5″ view port separates the components under vacuum (mirror, phosphor screen) and the components under atmosphere (lens, EMCCD). The phosphor screen size is 40 mm × 40 mm with a hole in the center. The mirror size is 40 mm × 56 mm with an elliptical hole of 6.5 mm × 9 mm. The distance between the center of the mirror to the lens entrance is 12 cm. The lens has a focal length of 40 mm and an *f*-number of 0.85. (b) and (c) are raw static diffraction patterns for nitrogen (b) and iodine (c), shown in logarithmic scale.

of the diffraction pattern at small angles. The pattern in Fig. 3b was captured with nitrogen, and is the configuration used for the time-resolved experiments described later in this manuscript. The pattern in Fig. 3c was captured with iodine molecules using the screen with the smaller hole. In the current detection system, the hole in the 45 degree mirror transmits a fraction of photons from the phosphor screen and thus creates non-uniformity in the low-s range of the diffraction patterns. This effect can be compensated by calibrating the image transfer function of the optical system, for example by using a static diffraction pattern from a known molecule.

3. Static gas electron diffraction with MeV electrons

Diffraction from molecules in the gas phase can be modelled using the independent atom approximation, and assuming the molecules are randomly oriented.[33] The transverse coherence of the electron beam is assumed to be larger than the size of the molecules but smaller than the distance between molecules. Thus, the scattering from different atoms within a molecule are added coherently, while the scattering from different molecules is added incoherently. Under these assumptions the scattering intensity $I(s)$ on the detector can be described as:

$$I(s) = I_0 \sum_{i=1}^{N} \sum_{j=1}^{N} f_i(s) f_j^*(s) \frac{\sin(r_{ij}s)}{r_{ij}s} \tag{2}$$

here $f_i(s)$ is the complex elastic scattering amplitude of the i^{th} atom in the molecule, r_{ij} is the distance between atoms i and j, I_0 is a constant and N is the total number of atoms in a molecule. The scattering is expressed in terms of the momentum change of the scattered electrons $s = \frac{4\pi}{\lambda}\sin(\theta/2)$, where θ is the scattering angle. The total scattering is typically separated into atomic scattering intensity I_{at} and a molecular scattering intensity I_{mol}:

$$I = I_{\text{at}} + I_{\text{mol,}} \tag{3}$$

$$I_{\text{at}}(s) = I_0 \sum_{i=1}^{N} \left| f_i(s) \right|^2, \tag{4}$$

$$I_{\text{mol}}(s) = I_0 \sum_{i=1}^{N} \sum_{j=1, j\neq i}^{N} f_i(s) f_j^*(s) \frac{\sin(sr_{ij})}{sr_{ij}}, \tag{5}$$

where the I_{mol} contains the interference terms from different atoms, and I_{at} acts like a background scattering that is modulated by I_{mol}. The scattering intensity decreases rapidly with s, so I_{mol} is rescaled to form the modified scattering intensity.

$$\text{sM}(s) = s\frac{I_{\text{mol}}}{I_{\text{at}}}. \tag{6}$$

Each pair of atoms will give rise to a sinusoidal modulation in sM(s), with the amplitude proportional to the product of the scattering amplitudes and inversely

proportional to the interatomic distance. For a diatomic molecule with interatomic distance r, the modified scattering becomes

$$\mathrm{sM}(s) = \frac{\sin(sr)}{r} \tag{7}$$

In this case a single sinusoidal modulation is present. In this formulation only elastic scattering is included. The inelastic scattering contributes to the experimental background but does not contain any structural information. The interatomic distance can be extracted either by a Fourier transform of sM or by fitting a sine function to the measured signal. Vibrational excitations within the electronic ground state are not taken into account in this formalism. The inclusion of vibration was found to be helpful for structural refinement in static gas electron diffraction,[30] but for UGED experiments the effect of vibrations is typically much smaller than the effect of structural rearrangements.

Experimentally, the sM must be extracted from a background of atomic scattering, inelastic scattering and background noise. The background noise is produced by electrons scattered towards the detector by collimating apertures or by background gas, by any background photons that reach the detector and by camera noise. Fig. 4a shows the different levels of background observed experimentally with nitrogen as the target molecule. The figure is obtained by azimuthally averaging a diffraction pattern, such as the one shown in Fig. 3b. Data below $s = 3$ Å^{-1} is not available due to the hole in the phosphor screen. The blue line in Fig. 4a shows the total counts on the detector, on a logarithmic scale. The image was acquired using 38k electrons per pulse at a repetition rate of 120 Hz and a total integration time of 30 minutes. The backing pressure on the nozzle was 1 bar, which results in an estimated sample density of 2×10^{17} molecules per cm^3. The green line in Fig. 4a shows the count levels when the experiment is run under the same conditions but with the gas jet off. The detected electrons are produced mostly by scattering from apertures and from the silicon nitride window. Scattering from the target gas is more than an order of magnitude stronger than the background. Finally, the magenta line shows the detector counts when both the gas jet and electron beam are turned off. This reflects

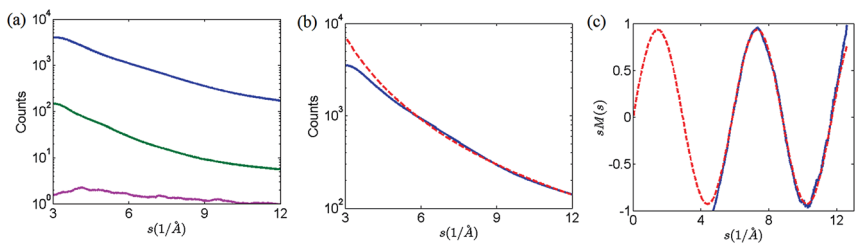

Fig. 4 Diffraction intensity of static N_2 molecules. (a) Azimuthally averaged diffraction intensity (blue), background taken without gas (green) and background taken without electron beam (magenta). The vertical axis is the raw camera counts per pixel per one minute integration time. (b) Azimuthally averaged diffraction intensity of static N_2 molecules (blue solid) and the scattering background obtained by a standard fitting routine (red dashed). (c) Experimental (blue solid) and simulated (red dashed) modified diffraction intensity sM(s). (c) is adapted from ref. 1

mostly the detector noise and is about three orders of magnitude below the scattering signal level.

The total experimental background needs to be removed from the data to extract the sM and the interatomic distance. We follow a standard iterative fitting procedure to remove the experimental background.[34] First, an initial guess of the bond length is used to simulate sM. The position of the zero crossings is extracted from the simulated sM. Then the background is determined by fitting an exponentially decaying function at these zero points, and the experimental sM is obtained by subtracting the fitted background. The error is calculated as the RMS difference between the experimental and simulated sM. The process is then repeated for a number of values of the bond length, until the best fit is found. Fig. 4b shows the total counts (blue line) and the fitted background (dashed red line), in logarithmic scale. Fig. 4c shows the experimental (blue line) and simulated (dashed red line) sM for the best fit parameter. The data below $s = 4$ Å^{-1} is missing in Fig. 4c because the zero crossing of sM is used to remove the background.

The bond length extracted from the sM in Fig. 4b is 1.073 ± 0.027 Å, in agreement with the previously measured bond length of nitrogen of 1.098 Å.[35] There is an uncertainty in the measurement of 2.5% due to the calibration of the sample to detector distance. The distance was calibrated using diffraction from a gold sample, and the uncertainty is caused by the scattering from the SiN window which makes the electron beam emittance larger. For time resolved experiments, if the ground state structure is known, a static gas diffraction pattern can be used as a calibration, reducing the uncertainties, as is shown later in this manuscript.

4. Finding the temporal overlap of electron and laser pulses

The temporal overlap, or time-zero, of the laser and electron pulses in UGED with keV electrons can be determined to an accuracy of 1 ps using plasma lensing.[22] The laser ionizes the sample molecules and the electron beam is deflected by the plasma fields as the charges separate. The deflection typically grows on a scale of picoseconds.[36,37] It was not clear whether this method could also be applied to relativistic electrons with MeV energies because they need higher fields to be deflected on the detector. We have seen, however, that the method works very well and time-zero can be determined with an accuracy of approximately 200 fs. We believe we see a strong effect because the laser and electron pulses are approximately collinear through the sample. We have not investigated the plasma deflection in detail to determine the relative contributions of electric and magnetic fields. We have characterized the changes on the electron beam and used it to find time-zero. Nitrogen is not an ideal candidate for plasma-lensing because it has a high ionization potential of 15.58 eV, nevertheless we are able to generate a sufficiently strong plasma by increasing the 800 nm Ti:sapphire fundamental laser intensity to 8×10^{14} W cm^{-2}. The laser focus spot size is 50 μm FWHM, and the electron beam is 200 μm FWHM at the interaction region. We expect that for molecules with a lower ionization potential a significantly lower laser intensity will be needed.

After traversing the laser plasma, the electron beam is deflected along the direction of the laser polarization. The effect is quantified by measuring the number of deflected electrons, *i.e.* electrons that are detected outside of the main beam. Fig. 5a shows the time trace obtained from a plasma lensing scan where the relative time delay between the electrons and laser is varied. Significant changes can be seen on a timescale of 200 fs. Fig. 5b shows an image of the electron beam without the plasma lensing effect, at a time of 100 fs before time-zero. Fig. 5c and d show the corresponding images of the beams for time delays of 400 fs and 900 fs after time zero, respectively. A significant number of electrons are deflected along the direction of laser polarization (vertical in the images). The white rectangle in Fig. 5c shows the region over which the deflected electrons are integrated.

5. Determination of temporal resolution and spatial resolution

We have used the rotational dynamics in nitrogen molecules to characterize the temporal resolution of the instrument. A femtosecond laser pulse with a wavelength of 800 nm is used to create a rotational wavepacket and impulsively align the molecules.[38] The laser pulse energy is 800 μJ, its duration 34 fs, and the laser focal size is 200 μm in diameter, resulting in a laser intensity of 5×10^{13} W cm^{-2}. When the molecules are aligned, the diffraction pattern becomes anisotropic,[7,39,40] and this anisotropy can be used to follow the temporal evolution of the angular distribution. We have chosen nitrogen for this experiment because the temporal evolution is very fast and dynamics of the alignment can be simulated

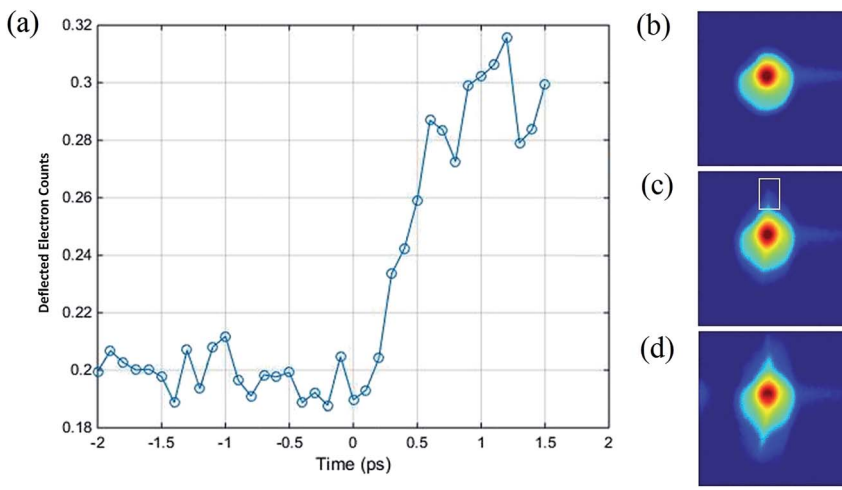

Fig. 5 Time-zero determined by plasma-induced lensing effect. (a) The deflected electron counts (normalized) as a function of delay time. Time-zero can be determined with an accuracy of approximately 200 fs. (b)–(d) Images of the electron beam on detector, at delay times of (b) −100 fs, (c) 400 fs and (d), 900 fs. The deflected electron counts shown in part (a) are calculated by summing over all the pixel counts in the white rectangular shape displayed in part (c). The plasma is generated by focusing an intense IR beam (8×10^{14} W cm^{-2}) on the N_2 gas jet.

accurately.[41,42] For example, the distribution changes from aligned (prolate) to anti-aligned (oblate) in 300 fs, and the fast changes can be used to accurately characterize the temporal resolution by comparing simulations and experiment.

Diffraction patterns were recorded as a function of delay between the alignment laser pulse and the probing electrons. The step size was 100 fs and the delay was varied from −1 ps to 10 ps, just over the time for the full revival of the alignment at 8.35 ps. The anisotropy of the diffraction pattern was determined for each time delay. Prior to this, each diffraction pattern was pre-processed by removing a dark background, finding the center of the diffraction pattern and normalizing to the total counts. The anisotropy was calculated by dividing the total counts in a horizontal cone with a half-angle of 35° by the total counts in a vertical cone with a half angle of 55°. A region of the pattern that shows high anisotropy, between $s = 3$ Å^{-1} and $s = 4.5$ Å^{-1}, was used for the calculation.

Fig. 6a shows the temporal evolution of the anisotropy in the diffraction pattern. The blue dots show the anisotropy extracted from the measured diffraction patterns. For each data point, the diffraction pattern was captured continuously for two minutes at a repetition rate of 120 Hz. In order to quantify the uncertainty in the anisotropy measurement, additional measurements were taken at a few points before time zero. The standard deviation for these points is displayed in Fig. 6a as error bars. The solid green and dashed red lines in Fig. 6a show the simulated anisotropy for two different sets of parameters. The angular distribution as a function of time was simulated using a rigid-rotor model.[42] A diffraction pattern was calculated from for each time delay, using the calculated angular distribution.[43] Finally, the anisotropy of the simulated pattern was calculated using the same procedure applied to the experimental data. The right hand axis of Fig. 6a shows the degree of alignment extracted from the simulation in terms of $\langle\cos^2\alpha\rangle$, where α is the angle between each molecule and the alignment axis, and the brackets indicate an ensemble average over all molecules. The

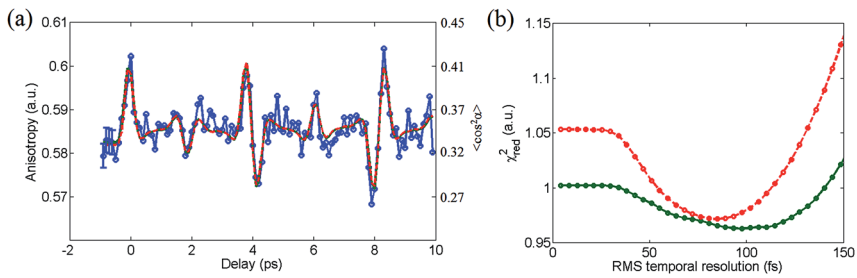

Fig. 6 Experimental anisotropy and χ^2 fitting. (a) Anisotropy evolution from experimental data (blue circles), simulation with values from the 2-parameter fit (dashed red line), and simulations with values from the 4-parameter fit (solid green line). (b) The reduced χ^2 metric for the 4-parameter fit (circles and solid green line) and 2-parameter fit (circles and dashed red line). The 4-parameter fit involves laser fluence, initial temperature, temporal resolution and a re-scaling factor that accounts for the excitation percentage of the target molecules. The 2-parameter fit uses the measured laser fluence and estimated initial temperature, while varying the temporal resolution and the re-scaling factor. The optimal temporal resolution from the 4-parameter fit and 2-parameter fit are 100 fs RMS and 85 fs RMS, respectively.

angular distribution changes rapidly with time, oscillating between alignment (increased anisotropy) and anti-alignment (decreased anisotropy).

The sharp feature around 4 ps corresponds to a half revival, while the feature around 8 ps corresponds to a full revival. The distribution changes very rapidly between the two extremes of maximum alignment (prolate distribution) and maximum anti-alignment (oblate distribution). The temporal evolution of the measured anisotropy signal is determined by three parameters: the initial temperature of the molecules, the fluence of the alignment laser pulse and the overall temporal resolution of the experimental set-up. The laser fluence was measured to be 2.0 J cm^{-2}. We estimated that the rotational temperature of the molecules in the jet before laser excitation was 65 K, based on the backing pressure, the electron-nozzle exit distance and the nozzle geometry.[44]

We have used a χ^2 fitting routine to extract the temporal resolution of the experiment, by comparing the data with the simulation results. The whole temporal scan shown in Fig. 6a is used for the fit. We performed the fit in two different ways, first fixing the values of the laser fluence and rotational temperature cited above, and then letting them also be free parameters in the fit. In the first case we run a two-parameter fit in which only the temporal resolution and a scaling factor were allowed to vary. The temporal resolution is introduced by convolving the simulated anisotropy with a Gaussian envelope. As the temporal resolution becomes longer in time, the fast-changing features in the anisotropy will start to disappear. The two-parameter fit returned a resolution of 85 fs RMS (200 fs FWHM) and scaling factor of 0.28 with a reduced χ^2 of 0.97. The rescaling factor of 0.28 means that 28% of the molecules were excited by the laser due to imperfect spatial overlap. The results of this fit are shown with the red circles in Fig. 6b. We also run a four-parameter fit in which the temporal resolution, scaling factor, laser fluence and the initial rotational temperature were allowed to vary. The fit returned a temporal resolution of 100 fs RMS (230 fs FWHM), laser fluence of 1.8 J cm^{-2}, rotational temperature of 54 K, scaling factor of 0.42 and reduced χ^2 of 0.96. The results are consistent with the two-parameter fit.

The changing angular distribution can be observed directly in the diffraction patterns. Fig. 7 shows the difference diffraction patterns corresponding to the peak alignment and peak anti-alignment. The difference diffraction patterns are generated by taking the difference between a diffraction pattern at a positive delay time (the electrons reach the sample after the laser) and a diffraction pattern at a negative time (the electrons reach the sample before the laser). For capturing high quality diffraction patterns, the integration time was increased to a total of 60 minutes for each pattern. Fig. 7a and b show the experimental and simulated difference patterns at the maximum alignment at the half revival (around 4 ps after laser excitation). There is good agreement between the experiment and simulation. The missing data in the experimental pattern (s < 3.5 Å) is filled in by letting the pattern smoothly go to zero at the center. The spatial resolution can be calculated from the maximum value of s captured in the experiment, $s_{max} = 8.3$ $Å^{-1}$, which gives a spatial resolution $\delta = 0.76$ Å.

Fig. 7c and d show the experimental and simulated 2D Fourier transform (FT) of the difference pattern. The FT shows the changes in the distribution of molecules in real space. For the prolate distribution, this means increased population along the direction of alignment and decreased population in the region perpendicular to the alignment. Since the FT gives a representation of the

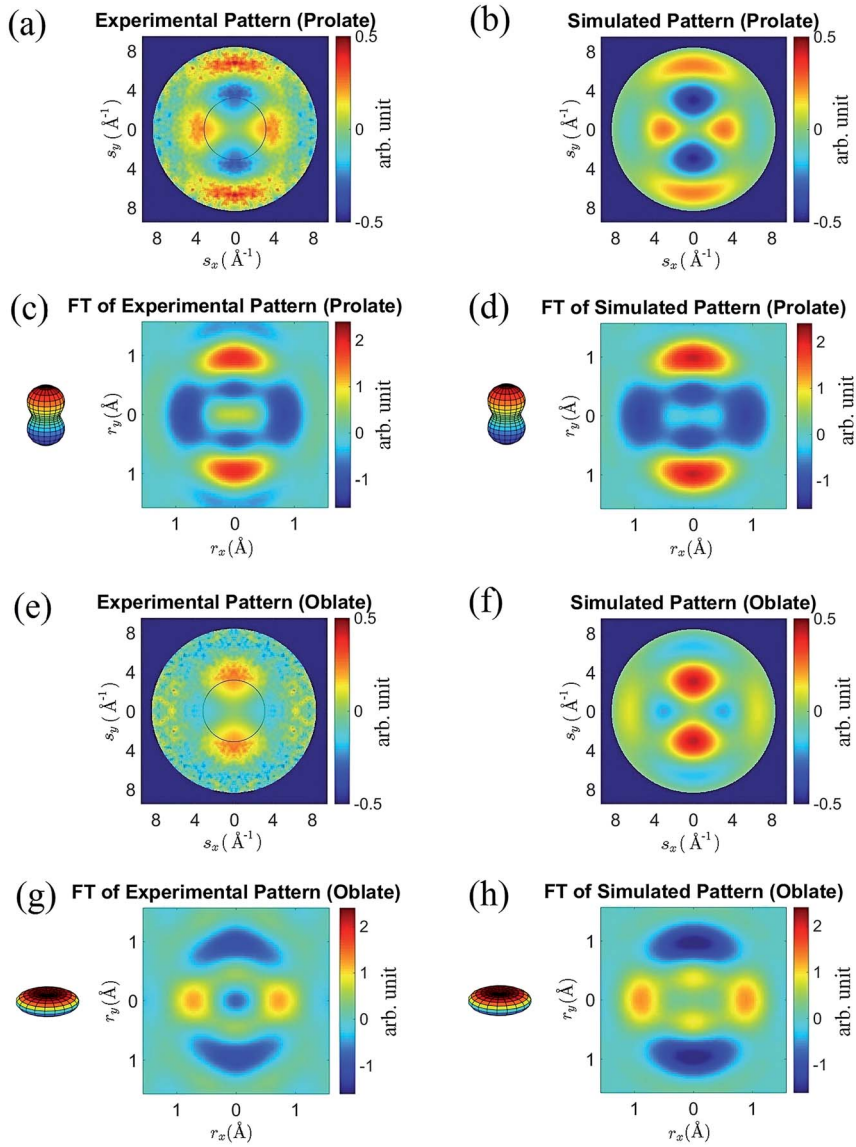

Fig. 7 2D N_2 diffraction patterns at half revival. (a) Experimentally measured and (b) simulated diffraction-difference patterns of the prolate distribution. (c) and (d) are Fourier transforms of (a) and (b), respectively. (e) Experimentally measured and (f) simulated diffraction-difference pattern of the oblate distribution. (g) and (h) are Fourier transforms of (e) and (f), respectively. In patterns (a) and (e), the data inside the black circles are missing due to the beam stop. They are obtained by extrapolating the pattern and letting the counts smoothly go to zero towards the center. For illustrative purpose, angular distributions are shown on the side of panel (c), (d), (g) and (h) for visual guidance. Figure is reproduced from ref. 1.

molecule in real space, the interatomic distance can be extracted from the diffraction patterns. The measured object is a 2D projection of a 3D distribution of molecules, so the interatomic distance is not equal to the distance of the bright

spots from the origin, as would be the case for perfectly aligned molecules. A least squares fitting method was used to extract the bond length form the real space object in Fig. 7c, using the static diffraction pattern as a calibration. The fitting was done by simulating the diffraction pattern for different bond lengths of nitrogen, and then finding the RMS difference between the simulated and measured objects. The angular distribution for the simulated patterns was extracted from the alignment simulation shown in Fig. 6a. The extracted bond length was 1.091 ± 0.011 Å, in good agreement with the ground state bond length of nitrogen of 1.098 Å.

Fig. 7e and f show the experimental and simulated difference diffraction patterns at the maximum anti-alignment during the half revival, where the distribution is oblate. In this case, there is increased population in the direction perpendicular to the alignment axis, as can be seen in the FTs in Fig. 7g and h. A similar fit for the bond length was performed, which returned a value of 1.096 ± 0.018 Å, in good agreement with the previous values. The fit was performed for ten different data sets (6 minutes of integration each), and the mean value is reported as the best estimate with the standard deviation of the mean reported as the uncertainty. Note that we had previously reported the uncertainty as the standard deviation,[1] but the standard deviation of the mean is a more accurate measure of the uncertainty. The experimental uncertainty in the bond length is significantly less than the spatial resolution of 0.76 Å. The resolution determines the width of the distribution along the radial direction (see Fig. 7c and d), while determining the bond length can be thought of as finding the center of the distribution (accounting for the fact that the alignment is not perfect). The resolution becomes important when there are multiple closely spaced distances to be measured simultaneously.

6. Conclusion and outlook

In summary, we have demonstrated that relativistic electrons can be used to break a longstanding barrier in the temporal resolution of gas phase electron diffraction. We have achieved a temporal resolution of 100 fs RMS (230 fs FWHM), and spatial resolution of 0.76 Å. Our results also show that for simple molecules the bond lengths can be determined with an accuracy significantly lower than the spatial resolution. These results open the door to imaging photo-induced chemical reactions in isolated molecules with a combined spatio-temporal resolution that will allow for resolving the motion of the nuclei on the sub-Å scale.

To further improve the spatial and temporal resolution, a number of system upgrades can be implemented in the near and far future. A direct detection sensor[45] will significantly reduce the detector noise, which will increase the SNR and thus the spatial resolution. The direct detection camera will also obviate the need for a 45 degree mirror with a hole, thus resolving the issue of a non-uniform transfer function and the missing data at small scattering angles. The signal levels could be further improved by replacing the circular orifice gas nozzle with a slit to generate a longer gas target. An RF-based compression cavity has been proposed to compress the pulse duration of MeV electron pulses down to the order of 10 fs.[46] The RF compression would also increase the number of electrons per pulse, thus to improving both the temporal and spatial resolution. Further improvements in temporal resolution require not only compressing the electron

pulses but also compensating the timing jitter. These could be achieved by measuring the TOA of each pulse and resorting the data on a shot-by-shot basis using time-stamping techniques.[47,48] Ultimately, a temporal resolution of 30 fs would be sufficient to capture most photochemical dynamics processes, but these improvements must be accompanied by an improvement of the spatial resolution such that small structural changes can be observed. With high spatio-temporal resolution, we can envision that this method will be able to capture not only structures, but also spatial information on the moving nuclear wavepackets. For example, as a reaction proceeds, the probability density of a nuclear wavepacket can broaden spatially, which can in principle be detected by UGED. It will be interesting to observe transition states where, on the relevant spatial and temporal scales, parts of a molecule may be delocalized.

There are several types of photo-reactions that could be studied with this setup, such as ultrafast relaxation, *cis–trans* isomerization, dissociation, and charge transfer. These reactions take place on femtosecond timescales, and in most cases the structure of the intermediate states has not been measured. Many of the molecules of interest have a low vapor pressure, so will only be available at densities well below the atmosphere. One of the major challenges will be to have a sufficiently high signal-to-noise ratio for structure retrieval.

We can make some estimates based on the nitrogen diffraction patterns presented in this manuscript. Here the sample was introduced into the nozzle with a backing pressure of approximately 1 bar and then entered the vacuum as an expanding gas jet. For many samples, the vapor pressure that can be expected (with some heating) to be on the order of 10 mBar, so the signal level (measured in scattered electrons per second) will decrease by a factor of a hundred. This decrease can be compensated by straightforward improvements in multiple components of the setup. One option is to increase the integration time of the diffraction patterns, but this is the least desirable route as the duration of the experiments will become very long and more susceptible to long term instabilities. In the current setup, the backing pressure that could be used was limited by the speed with which the gas could be pumped out of the system. With lower pressure in the nozzle (or more efficient pumping), the length of the gas jet could be increased by a factor of 2 to 5 without significantly degrading the temporal resolution. This would directly translate into 2–5 times more scattering. The repetition rate of the experiment can be increased from 120 Hz to 1 kHz with the current laser system, and it could be increased even further with an upgrade to the electron gun. This would result in an additional factor of 8 or more in average beam current. The use of RF compression, as mentioned above, can increase the charge of each pulse by a factor of 10 or more, also increasing the beam current and thus the total number of scattered electrons. Combining these improvements it is reasonable to expect a two order of magnitude increase in the signal level, opening the door to investigating a large number of possible target molecules.

Acknowledgements

The authors would like to thank SLAC management for the strong support. The technical support by the SLAC Accelerator Directorate, Technology Innovation Directorate, LCLS Laser Science & Technology division and Test Facilities

Department is gratefully acknowledged. This work was supported in part by the U.S. Department of Energy (DOE) Contract No. DE-AC02-76SF00515, DOE Office of Basic Energy Sciences Scientific User Facilities Division, the SLAC UED/UEM Initiative Program Development Fund, and by the AMOS program within the Chemical Sciences, Geosciences, and Biosciences Division of the Office of Basic Energy Sciences, Office of Science, U.S. Department of Energy. J. Yang, and M. Centurion were supported by the U.S. Department of Energy Office of Science, Office of Basic Energy Sciences under Award Number DE-SC0014170. M. S. Robinson was supported by the National Science Foundation EPSCoR RII Track-2 CA Award No. IIA-1430519. M. Guehr thanks the Volkswagen Foundation for a Lichtenberg Professorship.

References

1 J. Yang, *et al.*, Diffractive imaging of a rotational wavepacket in nitrogen molecules with femtosecond Megaelectronvolt electron pulses, *Nat. Commun.*, 2016, **7**, 11232.
2 A. A. Ischenko, J. D. Ewbank and S. Lothar, Structural kinetics by stroboscopic gas electron diffraction Part 1. Time-dependent molecular intensities of dissociative states, *J. Mol. Struct.*, 1994, **320**, 147–158.
3 J. D. Ewbank, *et al.*, Instrumentation for gas electron diffraction employing a pulsed electron beam synchronous with photoexcitation, *Rev. Sci. Instrum.*, 1992, **63**, 3352–3358.
4 C. Y. Ruan, *et al.*, Ultrafast diffraction and structural dynamics: the nature of complex molecules far from equilibrium, *Proc. Natl. Acad. Sci. U. S. A.*, 2001, **98**, 7117–7122.
5 H. Ihee, *et al.*, Direct imaging of transient molecular structures with ultrafast diffraction, *Science*, 2001, **291**, 458–462.
6 R. Srinivasan, J. S. Feenstra, S. T. Park, S. Xu and A. H. Zewail, Dark structures in molecular radiationless transitions determined by ultrafast diffraction, *Science*, 2005, **307**, 558–563.
7 C. J. Hensley, J. Yang and M. Centurion, Imaging of isolated molecules with ultrafast electron pulses, *Phys. Rev. Lett.*, 2012, **109**, 133202.
8 J. Yang, J. Beck, C. J. Uiterwaal and M. Centurion, Imaging of alignment and structural changes of carbon disulfide molecules using ultrafast electron diffraction, *Nat. Commun.*, 2015, **6**, 8172.
9 M. Centurion, Ultrafast imaging of isolated molecules with electron diffraction, *J. Phys. B: At., Mol. Opt. Phys.*, 2016, **49**, 062002.
10 M. Gao, *et al.*, Mapping molecular motions leading to charge delocalization with ultrabright electrons, *Nature*, 2013, **496**, 343–346.
11 T. Ishikawa, *et al.*, Direct observation of collective modes coupled to molecular orbital-driven charge transfer, *Science*, 2015, **350**, 1501–1505.
12 L. Waldecker, R. Bertoni and R. Ernstorfer, Compact femtosecond electron diffractometer with 100 keV electron bunches approaching the single-electron pulse duration limit, *J. Appl. Phys.*, 2015, **117**, 044903.
13 C. Gerbig, A. Senftleben, S. Morgenstern, C. Sarpe and T. Baumert, Spatio-temporal resolution studies on a highly compact ultrafast electron diffractometer, *New J. Phys.*, 2015, **17**, 043050.

14 T. Van Oudheusden, *et al.*, Compression of subrelativistic space-charge-dominated electron bunches for single-shot femtosecond electron diffraction, *Phys. Rev. Lett.*, 2010, **105**, 264801.
15 V. R. Morrison, *et al.*, A photoinduced metal-like phase of monoclinic vanadium dioxide revealed by ultrafast electron diffraction, *Science*, 2014, **346**, 445–448.
16 M. Gao, *et al.*, Full characterization of RF compressed femtosecond electron pulses using ponderomotive scattering, *Opt. Express*, 2012, **20**, 12048.
17 M. P. Minitti, *et al.*, Imaging Molecular Motion: Femtosecond X-Ray Scattering of an Electrocyclic Chemical Reaction, *Phys. Rev. Lett.*, 2015, **114**, 255501.
18 D. Rolles, *et al.*, Femtosecond x-ray photoelectron diffraction on gas-phase dibromobenzene molecules, *J. Phys. B: At., Mol. Opt. Phys.*, 2014, **47**, 124035.
19 C. I. Blaga, *et al.*, Imaging ultrafast molecular dynamics with laser-induced electron diffraction, *Nature*, 2012, **483**, 194–197.
20 M. G. Pullen, *et al.*, Imaging an aligned polyatomic molecule with laser-induced electron diffraction, *Nat. Commun.*, 2015, **6**, 7262.
21 M. Meckel, *et al.*, Laser-induced electron tunneling and diffraction, *Science*, 2008, **320**, 1478–1482.
22 M. Dantus, S. B. Kim, J. C. Williamson and A. H. Zewail, Ultrafast electron diffraction. 5. Experimental time resolution and applications, *J. Phys. Chem.*, 1994, **98**, 2782–2796.
23 P. Baum and A. H. Zewail, Breaking resolution limits in ultrafast electron diffraction and microscopy, *Proc. Natl. Acad. Sci. U. S. A.*, 2006, **103**, 16105–16110.
24 P. Zhang, J. Yang and M. Centurion, Tilted femtosecond pulses for velocity matching in gas-phase ultrafast electron diffraction, *New J. Phys.*, 2014, **16**, 083008.
25 S. P. Weathersby, *et al.*, Mega-electron-volt ultrafast electron diffraction at SLAC National Accelerator Laboratory, *Rev. Sci. Instrum.*, 2015, **86**, 073702.
26 S. Manz, *et al.*, Mapping atomic motions with ultrabright electrons: towards fundamental limits in space-time resolution, *Faraday Discuss.*, 2015, **177**, 467–491.
27 F. Fu, *et al.*, High quality single shot ultrafast MeV electron diffraction from a photocathode radio-frequency gun, *Rev. Sci. Instrum.*, 2014, **85**, 083701.
28 J. B. Hastings, *et al.*, Ultrafast time-resolved electron diffraction with megavolt electron beams, *Appl. Phys. Lett.*, 2006, **89**, 184109.
29 X. J. Wang, D. Xiang, T. K. Kim and H. Ihee, Potential of Femtosecond Electron Diffraction Using Near-Relativistic Electrons from a Photocathode RF Electron Gun, *J. Korean Phys. Soc.*, 2006, **48**, 390–396.
30 I. Hargittai and M. Hargittai, *Stereochemical Applications of Gas-Phase Electron Diffraction, Part A: Methods in Stereochemical Analysis*, Wiley-VCH, 1988.
31 J. Yang and M. Centurion, Gas-phase electron diffraction from laser-aligned molecules, *Struct. Chem.*, 2015, **26**, 1513–1520.
32 J. C. H. Spence, *et al.*, Diffraction and imaging from a beam of laser-aligned proteins: Resolution limits, *Acta Crystallogr., Sect. A: Found. Crystallogr.*, 2005, **61**, 237–245.
33 L. O. Brockway, Electron diffraction by gas molecules, *Rev. Mod. Phys.*, 1936, **8**, 231–266.

34 R. Srinivasan, V. A. Lobastov, C.-Y. Ruan and A. H. Zewail, Ultrafast electron diffraction (UED): A new development for the 4D determination of transient molecular structures, *Helv. Chim. Acta*, 2003, **86**, 1763–1838.
35 K. P. Huber and G. Herzberg, Molecular Spectra and Molecular Structure, *Constants of Diatomic Molecules*, Van Nostrand Reinhold Inc., 1979, vol. 4.
36 M. Centurion, P. Reckenthaeler, S. A. Trushin, F. Krausz and E. E. Fill, Picosecond electron deflectometry of optical-field ionized plasmas, *Nat. Photonics*, 2008, **2**, 315–318.
37 M. Centurion, P. Reckenthaeler, F. Krausz and E. E. Fill, Picosecond imaging of low-density plasmas by electron deflectometry, *Opt. Lett.*, 2009, **34**, 539–541.
38 H. Stapelfeldt and T. Seideman, Colloquium: Aligning molecules with strong laser pulses, *Rev. Mod. Phys.*, 2003, **75**, 543–557.
39 J. S. Baskin and A. H. Zewail, Oriented ensembles in ultrafast electron diffraction, *ChemPhysChem*, 2006, **7**, 1562–1574.
40 P. Reckenthaeler, *et al.*, Time-resolved electron diffraction from selectively aligned molecules, *Phys. Rev. Lett.*, 2009, **102**, 213001.
41 I. V. Litvinyuk, *et al.*, Alignment-dependent strong field ionization of molecules, *Phys. Rev. Lett.*, 2003, **90**, 233003.
42 J. Ortigoso, M. Rodriguez, M. Gupta and B. Friedrich, Time evolution of pendular states created by the interaction of molecular polarizability with a pulsed nonresonant laser field, *J. Chem. Phys.*, 1999, **110**, 3870–3875.
43 J. Yang, V. Makhija, V. Kumarappan and M. Centurion, Reconstruction of three-dimensional molecular structure from diffraction of laser-aligned molecules, *Struct. Dyn.*, 2014, **1**, 044101.
44 O. F. Hagena, Nucleation and growth of clusters in expanding nozzle flows, *Surf. Sci. Lett.*, 1981, **106**, 101–116.
45 M. Battaglia, *et al.*, Characterisation of a CMOS active pixel sensor for use in the TEAM microscope, *Nucl. Instrum. Methods Phys. Res., Sect. A*, 2010, **622**, 669–677.
46 R. K. Li, P. Musumeci, H. A. Bender, N. S. Wilcox and M. Wu, Imaging single electrons to enable the generation of ultrashort beams for single-shot femtosecond relativistic electron diffraction, *J. Appl. Phys.*, 2011, **110**, 074512.
47 M. Gao, Y. Jiang, G. H. Kassier and R. J. D. Miller, Single shot time stamping of ultrabright radio frequency compressed electron pulses, *Appl. Phys. Lett.*, 2013, **103**, 033503.
48 F. O. Kirchner, A. Gliserin, F. Krausz and P. Baum, Laser streaking of free electrons at 25 keV, *Nat. Photonics*, 2013, **8**, 52–57.